

Short-lived binary splits of an excited projectile-like fragment induced by transient deformation

A. B. McIntosh, S. Hudan, J. Black, D. Mercier, C. J. Metelko,* R. Yanez,† and R. T. de Souza‡

Department of Chemistry and Indiana University Cyclotron Facility 2401 Milo B. Sampson Lane, Bloomington, Indiana 47405, USA

A. Chbihi

GANIL, Caen, France

M. Famiano

Western Michigan University, Kalamazoo, Michigan, USA

M. O. Frégeau, J. Gauthier, J. Moisan, and R. Roy

Université Laval, Québec, Canada

S. Bianchin, C. Schwarz, and W. Trautmann

GSI Helmholtzzentrum GmbH, Planckstr. 1, D-64291 Darmstadt, Germany

(Received 7 September 2009; published 5 March 2010)

Aligned fragment emission associated with peripheral and midperipheral dissipative collisions of $^{124}\text{Xe} + ^{124}\text{Sn}$ at $E/A = 50$ MeV is examined. Binary decay of the excited projectile-like fragment (PLF*) is correlated with significant velocity damping from the projectile velocity. Both a forward emission component, attributed to standard statistical emission, and a backward component are observed. The backward component arises from both statistical and dynamical decay processes. This backward component manifests a strong alignment with the direction of the PLF* velocity and is found to depend sensitively on the atomic number of the light fragment, Z_L , and the velocity of the PLF*. The yield of the backward component is significantly enhanced relative to the forward component. The composition of fragments emitted in the backward direction reveals that a correlation between alignment and neutron excess exists for fragments with $Z < 8$. From the measured asymmetry of the angular distributions, the angular distribution for dynamical fragment emission is deduced. Comparison with a schematic one-dimensional Langevin model allows extraction of both the magnitude and the dependence on Z_L of the transient initial deformation of the PLF*. Fragment emission times of the order of $0.25\text{--}1.5 \times 10^{-21}$ s are extracted.

DOI: [10.1103/PhysRevC.81.034603](https://doi.org/10.1103/PhysRevC.81.034603)

PACS number(s): 25.70.Mn, 25.70.Lm

I. INTRODUCTION

Dynamical decay of nuclei provides a window into the interplay between collective modes and thermal modes. At low excitation energy, ternary fission provides the classic example of dynamical fragment production [1]. The characteristic energy and angular distributions of intermediate mass fragments, $3 \leq Z \leq 20$, provide distinct evidence that these fragments originate from the neck region (between the separating fission fragments) as the fission proceeds [1–3]. For low incident energy, however, the coupling between the incident collective motion and the collective motion responsible for the dynamical breakup of the system is weak. Consequently, spontaneous or induced fission at low incident energies occurs with low probability [4]. However, simulations indicate that introduction of additional kinetic energy along the scission direction can significantly enhance the probability

of ternary fission as well as modify the characteristics of the ternary particle [5]. Enhanced coupling of the entrance channel collective motion into the fission degree of freedom, conditions that exist at intermediate energies could result in increased ternary breakup [6]. At intermediate energies, noncentral collisions of two heavy ions have been observed to result in copious production of fragments [6–18] with velocities intermediate between the projectile-like and target-like nuclei.

The observation of these fragments has been associated with the breakup of noncompact cylindrical geometries [8] which manifest a strong alignment with the direction of the projectile-like fragment, indicating a dynamical origin [12,13,19]. Moreover, a correlation between parallel velocity order and average fragment size is observed [16]. This dynamical component increases in yield with increasing incident energy [11]. The width of the observed angular distributions [7] or energy-angle correlations [6] for this process can be used to extract a lifetime. In addition, it has been observed that the neutron-richness of the dynamical fragments increases as they become more energetic [20]. An alternate description of these nonisotropic decay patterns has been related to the Coulomb influence of the target-like fragment on the statistical decay of the projectile-like fragment [21]. The impact of this influence is largest for the emissions which occur when

*Present address: Particle Physics Dept., Rutherford Appleton Labs., Didcot, UK.

†Present address: Department of Chemistry, Oregon State University, Corvallis, OR, 97331, USA.

‡desouza@indiana.edu

the PLF* and TLF* are in proximity, indicating that this nonisotropic pattern is indicative of early emissions. Despite the characterization of short-lived (dynamical) decay in several independent experiments for various systems, many aspects of this prompt fragment production remain poorly understood. The present work provides new information on this decay mode.

When the matter distributions of two colliding heavy ions overlap, mass, charge, and energy are exchanged. For such collisions a binary dissipative process occurs which results in the production of an excited projectile-like fragment (PLF*) and an excited target-like fragment (TLF*). The magnitude of the excitation of the two nuclei is associated with the velocity damping observed in the collision [22]. Due to their relative kinetic energy and angular momentum, however, the two reaction partners are forced to separate having undergone only a fraction of a rotation. As they separate, the excited PLF* and TLF* deexcite. The time scale of their decay depends on their excitation as well as their transient deformation and any large amplitude collective motion. Fragments can be produced as the system evolves from the shortest times where the reaction dynamics dominate to the long times where the standard statistical decay of the PLF* and TLF* dominates. Consequently, the decay of the system reflects the interplay of standard statistical emission together with the reaction dynamics.

II. EXPERIMENTAL SETUP

The experiment was conducted at the GANIL facility in Caen, France, where beams of $^{124,136}\text{Xe}$ ions accelerated to $E/A = 50$ MeV impinged on $^{112,124}\text{Sn}$ targets with an average beam intensity of $\approx 10^8$ p/s. Charged products of the reaction were identified by two detector arrays located within a thin-wall aluminum scattering chamber. One array, FIRST [23], consisting of annular segmented silicon detectors backed by CsI(Tl) crystals with photodiode readout, subtended the angular range $3^\circ \leq \theta_{\text{lab}} \leq 14^\circ$. The most forward telescope in FIRST, designated T1, spanned the angular range $3^\circ \leq \theta_{\text{lab}} \leq 7^\circ$ and provided identification by atomic number of all products up to $Z = 55$. In addition, it allowed isotopic information for $Z \leq 14$. This telescope consisted of a Si(IP)-Si(IP)-CsI(Tl)/PD stack in which the silicon detectors were $270 \mu\text{m}$ thick and $1000 \mu\text{m}$ thick. Both silicon detectors in T1 had 48 concentric rings on the junction side and 16 pie-shaped sectors on the ohmic side (S2 design) [24]. The larger angle telescope in FIRST, designated T2, was a Si(IP)-CsI(Tl)/PD stack with a $500\text{-}\mu\text{m}$ -thick silicon S1 design detector [24] as the first element. This detector has 16 rings further subdivided into four quadrants on the junction side along with 16 pie-shaped sectors on the ohmic surface [24]. Each CsI(Tl) crystal in T1 and T2 matched the pie-shaped geometry of the silicon detector in front of it. The high segmentation of FIRST provided an angular resolution of $\pm 0.05^\circ$ ($3^\circ \leq \theta_{\text{lab}} \leq 7^\circ$) and $\pm 0.23^\circ$ ($7^\circ \leq \theta_{\text{lab}} \leq 14^\circ$) in polar angle and $\pm 11.25^\circ$ in azimuthal angle. The large number of analog signals from these detector segments were processed with multiplexed analog shaping electronics (MASE) [25]

and subsequently digitized. The obtained energy resolution of 0.5% was characteristic of this type of detector. Charged particles emitted at larger laboratory angles were identified in the LASSA array [26] which provided isotopic identification of fragments for $Z \leq 8$. This charged particle experimental setup provided good characterization of fragments forward of the center of mass of the system. All our subsequent analysis is therefore restricted to fragments emitted forward of the system's center of mass. Neutrons emitted in this experiment were identified by 27 detectors of the DEMON array [27]; however, the neutron data are not utilized in the present analysis.

III. EXPERIMENTAL RESULTS

A. Overview of the reaction

An overall perspective of the collisions selected, $^{124}\text{Xe} + ^{124}\text{Sn}$ at $E/A = 50$ MeV, is provided in the left-hand panel of Fig. 1, which examines the correlation between the atomic number and laboratory velocity of the heaviest fragment measured in the angular range $3^\circ \leq \theta_{\text{lab}} \leq 7^\circ$. Clearly evident is a dominant peak at $Z = 54$ and $V = 9.4$ cm/ns corresponding to elastically and quasielastically scattered particles. Moreover, as the atomic number decreases a distinct peak in velocity is evident for all size fragments. The most probable velocity for each Z , indicated by the solid circles in the figure, shows an initial decrease followed by a saturation around 9 cm/ns. Along this ridge one observes a decrease in yield in the quasielastic regime followed by a minimum at $Z \approx 45$ and a peak at $Z \approx 27$. Additionally, one observes that the width of the velocity distribution increases with decreasing Z , particularly in the direction of lower velocities. The velocity damping observed from $Z = 54$ to $Z = 45$ is qualitatively consistent with a binary dissipative scenario [28].

The excited heavy fragments produced in the dissipative binary collision can subsequently deexcite by undergoing fission or via evaporation of nucleons or clusters. While at energies near the Coulomb barrier the PLF* and TLF* achieve nearly full thermal equilibration prior to undergoing statistical

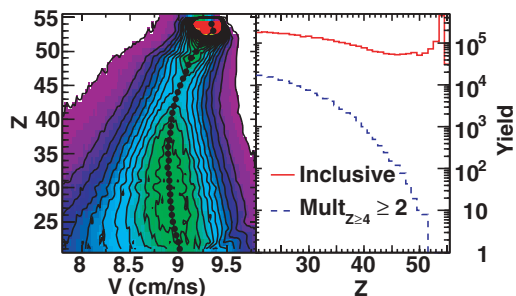


FIG. 1. (Color online) (Left panel) Two-dimensional distribution of the yield (linear scale) as a function of atomic number of the heaviest fragment and its velocity in the laboratory frame in the angular range $3^\circ \leq \theta_{\text{lab}} \leq 7^\circ$. (Right panel) Comparison of the inclusive Z distribution measured together with the Z distribution selected on the detection of two fragments with $Z \geq 4$ in the same angular range.

decay, the amount of particle emission which precedes equilibration increases with increasing incident energy [11]. This nonequilibrium decay of the PLF* is characterized by a strong alignment with the PLF*-TLF* separation axis and has been interpreted [8,12,13,16] as the dynamical breakup of a binary system with an elongated necklike structure reminiscent of ternary fission.

In the right-hand panel of Fig. 1 the inclusive Z distribution is shown. In addition to the prominent elastic peak at $Z = 54$, for $Z \leq 45$ a significant yield exists which increases with decreasing Z . We also examine the Z distribution for events in which two fragments both with $Z \geq 4$ are observed in the angular range $3^\circ \leq \theta_{\text{lab}} \leq 7^\circ$. This two fragment requirement eliminates the peak at $Z = 54$ due to the suppression of elastic and quasielastic processes indicating that at least a minimum energy dissipation has occurred for these $M \geq 2$ events. The Z distribution of the heavy particle for these events rises with decreasing Z and seems to reach a maximum in the vicinity of $Z = 20$. For the Z distribution associated with $M \geq 2$, the rapid increase in yield with decreasing Z suggests that for the inclusive distribution the increase in the yield with decreasing Z when $Z \leq 45$ is likely associated with two (or more) fragments produced forward of the system's center of mass. The remainder of this analysis will focus on the largest two fragments measured in the angular range $3^\circ \leq \theta_{\text{lab}} \leq 7^\circ$.

In Fig. 2 we examine the parallel velocity distributions along the beam axis associated with the detection of at least two fragments with $Z \geq 4$ in the angular range $3^\circ \leq \theta_{\text{lab}} \leq 7^\circ$. The heaviest two fragments are distinguished on the basis of their atomic number and referred to as Z_L and Z_H for the light fragment and heavy fragment, respectively. Representative velocity distributions for $Z_L = 5, 8, 11$, and 14 are depicted. For $Z_L = 5$, one observes that the heavy fragment manifests a

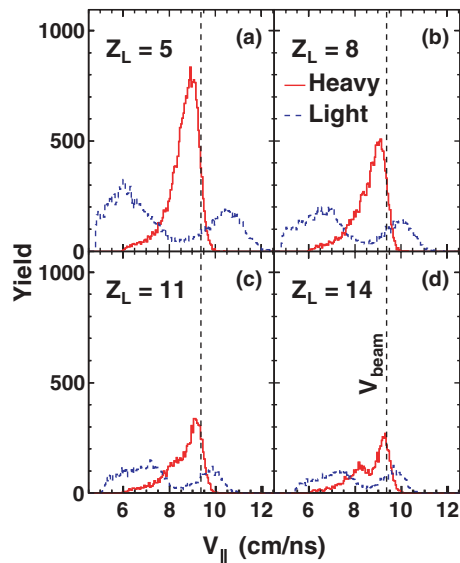


FIG. 2. (Color online) Parallel velocity distributions for both fragments detected in $3^\circ \leq \theta_{\text{lab}} \leq 7^\circ$. The velocity distribution of the heavy fragment is shown in a solid (red) line; that of the light fragment is shown as a dashed (blue) line. Different panels correspond to light fragments with different atomic number as indicated.

velocity distribution peaked at ≈ 9 cm/ns which is slightly damped from the beam velocity ($V_{\text{beam}} = 9.39$ cm/ns). In contrast, the parallel velocity of the light fragment is bimodal in nature with peaks at $V = 6$ and 10.5 cm/ns roughly centered on the most probable velocity of the heavy fragment. It is important to realize that the low velocity Z_L is peaked well above midvelocity ($V = 4.81$ cm/ns). Similar distributions are observed in the case of $Z_L = 8$ and 11 . In the case of $Z_L = 14$, however, one observes that the velocity distribution of the heavy fragment has a lower velocity shoulder peak located at ≈ 8.5 cm/ns. Closer examination of the $Z_L = 11$ case reveals that this lower velocity component for the heavy fragment also exists for this case. It is reasonable to conclude that this low-velocity component is also present for smaller Z_L in the low-velocity tail of the associated distribution.

The origin of the bimodal velocity distribution in the case of Z_L is easily understood. Binary decay of the PLF* in the angular range $3^\circ \leq \theta_{\text{lab}} \leq 7^\circ$ selects primarily forward and backward emission in the PLF* frame. “Forward” emission is associated with parallel velocities $V_L > V_H$ while “backward” emission is associated with $V_H > V_L$. Recoil effects which increase as Z_L increases are responsible for the bimodal nature of V_H . The observation of these recoil effects indicates that Z_H and Z_L are correlated and originate from a common parent. While midvelocity fragments have been the focus of previous studies [11,20,29,30], in this work we examine fragment emission centered on the projectile velocity.

Distributions of the relative velocity, V_{REL} , and the velocity of the center of mass of this fragment pair, $V_{\text{c.m.}}$, are presented in Fig. 3. We have further categorized the events into the cases of forward, $V_L > V_H$, and backward, $V_H > V_L$, emission based on the magnitudes of their velocities. The first noteworthy feature for both the V_{REL} and $V_{\text{c.m.}}$ distributions is that the yield associated with the backward emission component (blue symbols) significantly exceeds that of the forward emission component (red symbols), a result consistent with previous work [13]. In the case of forward emission, designated by the red symbols, the most probable V_{REL} is 2.05 cm/ns, in approximate agreement with fission [31] and evaporation [32] systematics, indicating a Coulomb dominated evaporative scenario. The distribution of V_{REL} for backward emission

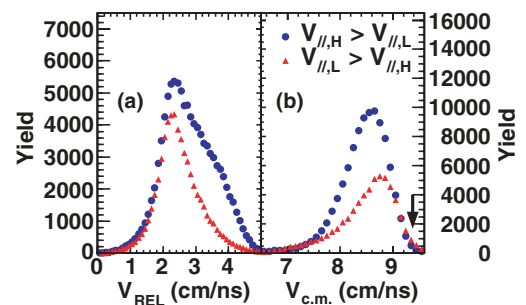


FIG. 3. (Color online) (Left column) Relative velocity distributions between the light and heavy fragment for the case of forward emission (red symbols) and backward emission (blue symbols). (Right column) Center-of-mass velocity of the Z_L and Z_H pair selected on forward and backward decay. The arrow designates the beam velocity.

extends to somewhat larger velocities and is peaked at $V_{\text{REL}} = 2.25$ cm/ns. These somewhat larger velocities may indicate the presence of collective dynamics in the backward direction and possibly higher emission temperatures. In the right-hand panel of Fig. 3, the distributions of the center-of-mass velocity of the fragment pair are compared for the forward and backward cases. Both distributions exhibit similar damping with respect to the beam velocity (indicated by the arrow), although the most probable $V_{\text{c.m.}}$ associated with backward emission is somewhat smaller than that associated with forward emission, indicating a larger degree of damping for backward decay. Both distributions are Gaussian-like with tails extending to lower $V_{\text{c.m.}}$ with comparable widths although for the forward emission a larger fraction of the distribution exists at low velocities as compared to backward emission.

In Fig. 4 we examine the correlation between the most probable velocity of the two-fragment center of mass, $V_{H+L,\text{peak}}$ and the total atomic number, $Z_H + Z_L$. For reference we also show the most probable velocity of the heavy fragment in the inclusive case. For the inclusive case, starting from the projectile at $Z = 54$ one observes the damping of the PLF with decreasing atomic number as was first evident in the left-hand panel of Fig. 1. From essentially beam velocity (≈ 9.4 cm/ns) the heavy fragment velocity decreases to 8.9 cm/ns. For the smallest heavy fragments measured, the fragment velocity increases slightly to ≈ 9 cm/ns. A similar saturation in the damping for projectile-like fragments has been previously observed in heavy-ion collisions of Kr projectiles with Sn and Ni nuclei at 25 MeV/nucleon [33] and Au+Au at 1 GeV/nucleon [34]. In comparison to the inclusive case, the two fragment cases are substantially more damped for all Z . A noteworthy feature of Fig. 4 is the similarity of the damping observed for both forward and backward emission. To first order, the damping in both cases is the same with the backward emission exhibiting a slightly larger damping over the range shown consistent with the integrated trend observed

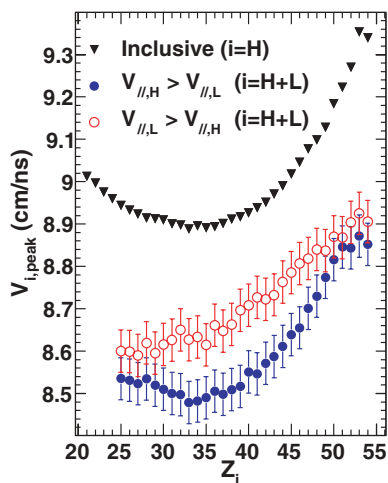


FIG. 4. (Color online) Dependence of the most probable velocity of the system composed of $Z_H + Z_L$ as a function of the total atomic number of the pair. For comparison, the dependence of the velocity of the heavy fragment on its atomic number in the inclusive case is also shown.

in the right-hand panel of Fig. 3. The slope of the most probable velocity with Z for the two fragment case with $Z \geq 35$ is also comparable to that for the inclusive case although slightly less than the dissipation rate observed for the most peripheral collisions. The similarity of the dissipation observed for both forward and backward emission provides supporting evidence that Z_H and Z_L originate from a common parent.

B. Angular distributions

To examine these decays in more detail we construct the relative angle, α , between the center of mass and relative velocity vectors of the fragment pair such that $\cos(\alpha) = +1$ corresponds to the case of complete alignment with $V_H > V_L$. The measured distributions of $\cos(\alpha)$ selected on Z_L are shown in Fig. 5 as the shaded histograms. The red line, which shows the result of an isotropic emission simulation, will be subsequently discussed. For small values of Z_L the angular distribution is strongly peaked in the backward direction, indicating a strong alignment of the V_{REL} and $V_{\text{c.m.}}$ vectors. Such strong alignment is not evident for the forward emission [$\cos(\alpha) < 0$]. With increasing Z_L , the angular distribution becomes more symmetric. In addition, one observes that the width of the angular distribution in the backward direction increases with increasing Z_L , revealing a decreased degree of alignment. The strong alignment of “midvelocity” fragments has been previously noted [12,13,16,17] and attributed to

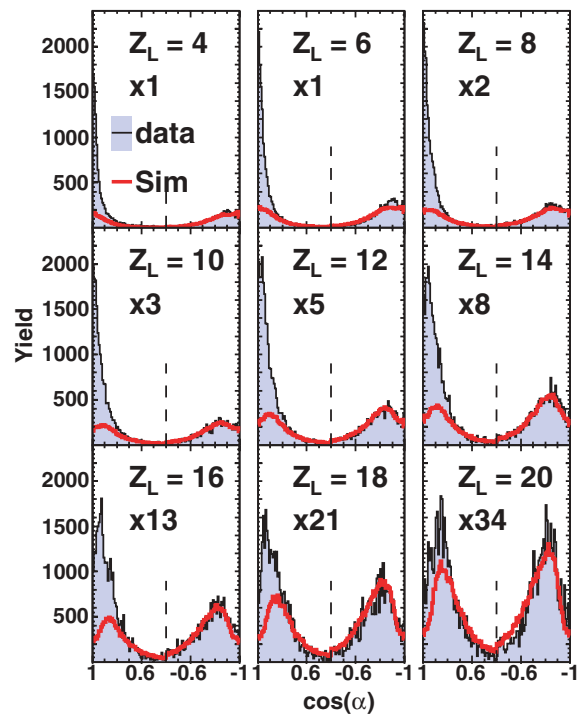


FIG. 5. (Color online) Angular distributions of the orientation of the binary splits Z_L-Z_H relative to the direction of their center-of-mass velocity. Distributions of $\cos(\alpha)$ for different Z_L are shown. Note the orientation of the abscissa, which puts the backward emission on the left. The measured yield for different Z_L has been multiplied by the factor shown in each panel for presentation purposes.

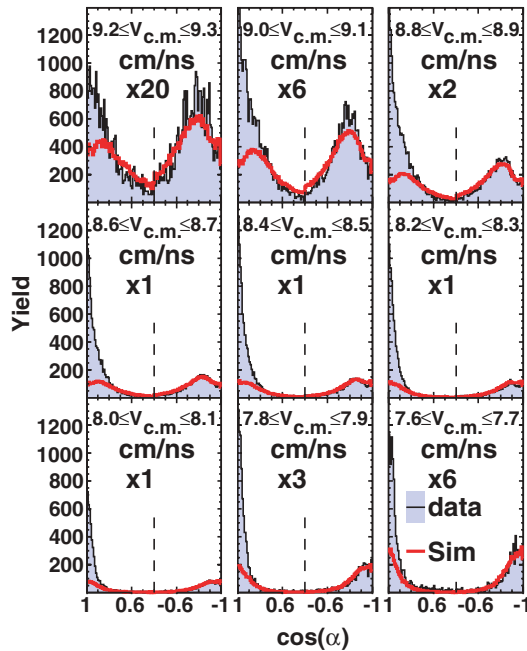


FIG. 6. (Color online) Distributions of $\cos(\alpha)$ for selected ranges of $V_{c.m.}$.

the breakup of a deformed PLF* or necklike configurations. It is remarkable, however, that even for fragments as large as $Z_L = 18$ an asymmetry between forward and backward emission is observed. The systematic evolution of this decay mode with fragment size and indeed its persistence for large fragments is a noteworthy characteristic.

The dependence of the $\cos(\alpha)$ on $V_{c.m.}$ is presented in Fig. 6. It is clear that for low-velocity dissipation, $9.2 \leq V_{c.m.} \leq 9.3$ cm/ns, the measured angular distribution (shaded histogram) is approximately forward-backward symmetric. For slightly larger velocity dissipation, $9.0 \leq V_{c.m.} \leq 9.1$ cm/ns, the onset of the backward aligned component is observed. As the $V_{c.m.}$ decreases further the width of the backward distribution decreases significantly, indicating that the degree of alignment is more pronounced. This feature of aligned decay persists even for the largest damping presented.

C. Isotopic distributions

One probe of the degree of equilibration attained in heavy-ion collisions is the composition of fragments produced in the collision. Shown in Fig. 7 as histograms are the isotopic distributions for different Z_L fragments between $Z_L = 6$ and $Z_L = 11$. For presentation purposes, the yield distributions are scaled by the factors indicated in the figure. To extract the yields of individual isotopes we have performed multi-Gaussian fits of the isotopic distributions. The resultant fits are shown as the solid (blue) line which is superimposed on the histograms. In the left-hand and center columns of the figure, the distributions for C and O fragments are depicted with selection on the alignment $\cos(\alpha)$ as indicated in the figure. If one examines the yield for ^{12}C and ^{14}C one observes that the most aligned case, $\cos(\alpha) > 0.97$, favors production of ^{12}C as compared to ^{14}C . This difference is reduced with decreasing alignment. In contrast, for oxygen isotopes, with decreasing alignment, the “neutron-poor” ^{16}O isotope is favored over the “neutron-rich” ^{18}O . These changes in the isotopic distribution with alignment indicate sensitivity to the nonequilibrium features of the rotating source. To illustrate the quality of the isotopic information for $Z_L > 8$ we show, in Figs. 7(g), 7(h), and 7(i), isotopic yields for $Z_L = 9-11$. The relative integrated yields extracted for $Z_L = 3-17$ are shown in Table I.

Having extracted the isotopic yields we calculate the $\langle N \rangle - Z$ of the light fragment as a function of Z_L selected on $\cos(\alpha)$. The data presented in Fig. 8 are remarkably clustered into two groups. For $Z_L < 9$ the fragments manifest a value of $\langle N \rangle - Z$ between ≈ 1.0 to 1.2 with the exception of carbon fragments which are associated with a smaller value of $\langle N \rangle - Z$. In contrast, $Z_L \geq 9$ exhibit a larger value of $\langle N \rangle - Z$, typically 1.45–1.65. The abrupt change in $\langle N \rangle - Z$ at $Z_L = 9$ is marked. One also observes that the more aligned component (closed symbols) manifests a slightly lower $\langle N \rangle - Z$ than the less aligned component (open symbols) for all fragments with the exception of oxygen. This difference in composition as a function of alignment is larger for $Z_L < 8$ than for $Z_L \geq 9$. This dependence of $\langle N \rangle - Z$ on $\cos(\alpha)$ indicates that chemical equilibrium is *not* achieved in these binary breakups.

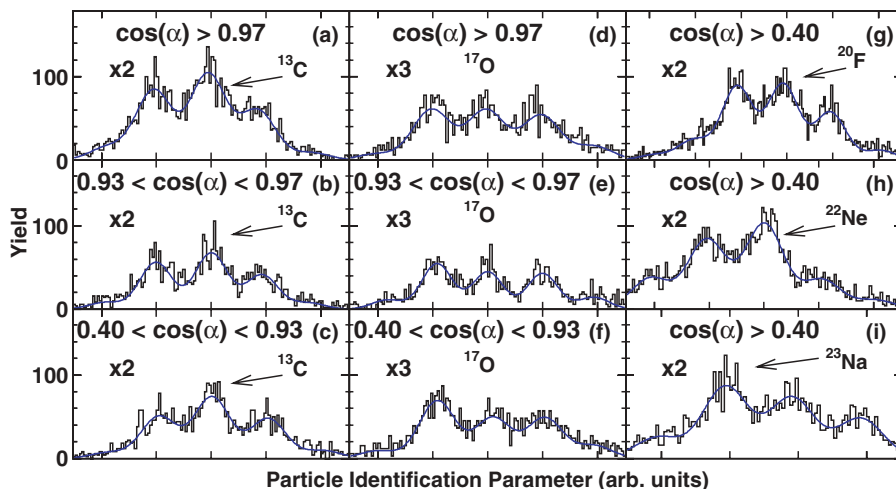


FIG. 7. (Color online) Mass distributions for $Z_L = 6-11$ fragments gated on the emission direction. Distributions have been scaled by the factors indicated for presentation purposes.

TABLE I. Isotopic yield of backward emitted Z_L fragments expressed as a percentage. The measured yield for each Z_L is shown in the second column. The yields presented are integrated over the interval $0.4 \leq \cos(\alpha) \leq 1.0$

		$N_L =$														
		3	4	5	6	7	8	9	10	11	12	13	14	15	16	17
$Z_L = 14$	$Y = 4216$												13.6	30.2	36.6	19.6
$Z_L = 13$	$Y = 4649$											9.79	37.3	36.4	16.5	
$Z_L = 12$	$Y = 5741$										16.9	30.4	35.2	17.5		
$Z_L = 11$	$Y = 6244$									10.8	38.2	30.4	20.7			
$Z_L = 10$	$Y = 7254$								13.2	30.6	39.0	11.9	5.35			
$Z_L = 9$	$Y = 7240$						3.58	8.04	30.8	32.6	19.6	5.35				
$Z_L = 8$	$Y = 9745$					5.30	32.5	27.5	26.0	8.78						
$Z_L = 7$	$Y = 12133$				3.07	18.5	55.4	14.5	8.54							
$Z_L = 6$	$Y = 15912$			5.61	29.8	37.6	23.2	3.77								
$Z_L = 5$	$Y = 14576$			19.1	57.8	16.4	6.70									
$Z_L = 4$	$Y = 11844$	9.63		48.1	42.3											

D. Modeling the isotropic component

The observation of an anisotropic angular distribution can be related to the decay of a nonspherical source for which the decay lifetime is short relative to the rotational period [7,17]. A relatively isotropic emission pattern has been observed [22,35] in the case of forward emission ($V_L > V_H$). This isotropic emission must also contribute to the case of backward emission. In addition to the isotropic emission component, an aligned component also exists corresponding to the short-lived (dynamical) decay of the PLF*. In order to quantitatively examine this short-lived (dynamical) decay component it is necessary to subtract the longer-lived isotropic component from the measured yield. To accomplish this subtraction, we have constructed a simple model which utilizes the forward emission as a reference. We subsequently filter the results of the simulation through a software filter of the

experimental apparatus. This software filter accounts for the geometrical acceptance, thresholds, and the finite granularity of the detectors. In this manner, we account for the slightly different experimental acceptance associated with forward and backward emission.

In this simple model, we sample the experimental distributions associated with forward emission to provide reasonable initial distributions for the parent PLF*. The size of the parent PLF* is chosen by sampling the experimental two dimensional distribution of Z_H vs. Z_L . Given the atomic number of each fragment, the mass number is determined from the evaporation attractor line systematics [36]. The atomic number and mass number of the PLF* is calculated to be the sum of the atomic and mass numbers, respectively, of the two individual fragments. To determine the velocity of the PLF* we sample the $V_{c.m.}$ distribution for the selected Z_{H+L} . The deflection angle from the beam direction, θ_{H+L} is sampled in the same fashion with all azimuthal angles for the PLF* taken to be equally probable. Having determined the velocity vector of the PLF*, the reaction plane is defined by this velocity vector and the beam direction. The relative velocity of the two fragments is then sampled from a Gaussian, with a centroid given by the Viola systematics and with a Z_L -dependent width taken from experimental data. All emission angles of the Z_L fragment from the PLF* in the reaction plane are taken to be equally probable consistent with the decay of a rotating source. The out-of-plane angle, ϕ is sampled from a distribution described by $P(\sin\phi) = A \exp(-\omega^2 \sin^2\phi)$. This formalism has been previously used to describe out-of-plane particle emission [37].

The results of the simulation (filtered by the experimental acceptance) are shown in Figs. 5 and 6 as the solid (red) line. As expected, the simulation provides a reasonably good description of the forward emission. Comparison of the simulation in the forward and backward directions shows that the experimental acceptance results in a somewhat asymmetric angular distribution. The observed asymmetry in the data, however, clearly cannot be explained only in terms of isotropic emission after accounting for the detector acceptance.

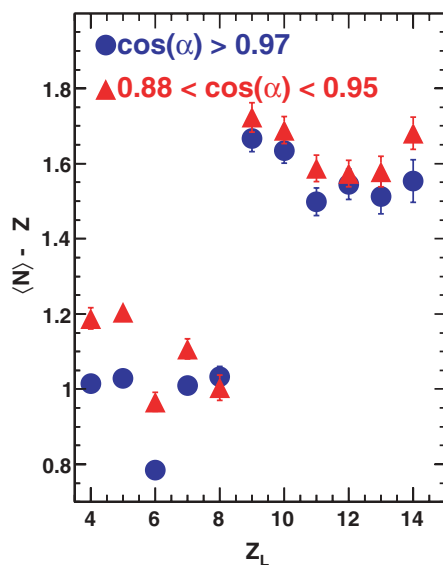


FIG. 8. (Color online) Average $N-Z$ of the light fragment as a function of Z_L selected on $\cos(\alpha)$.

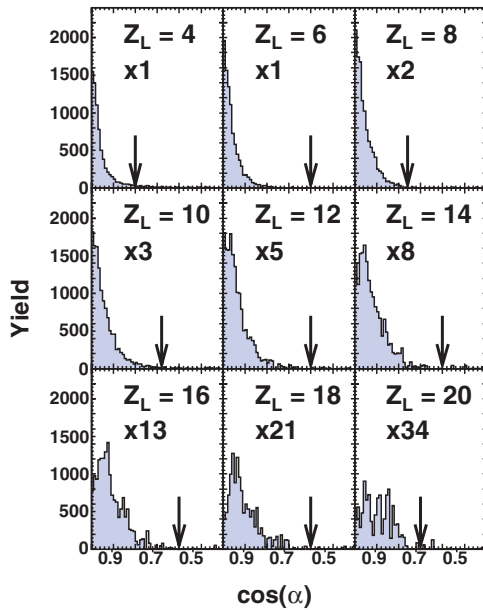


FIG. 9. (Color online) Distributions of $\cos(\alpha)$ corresponding to the difference between the measured backward emission and the simulation of statistical emission for different values of Z_L .

E. Characterizing the dynamical component

The difference between the measured backward yield and the simulated emission in the backward direction is shown in Fig. 9 for different representative Z_L and Fig. 10 for different representative $V_{c.m.}$. As expected from the raw experimental distributions, the width of the angular distributions increase with increasing Z_L and decrease with increasing damping. The yields and second moments of these angular distributions

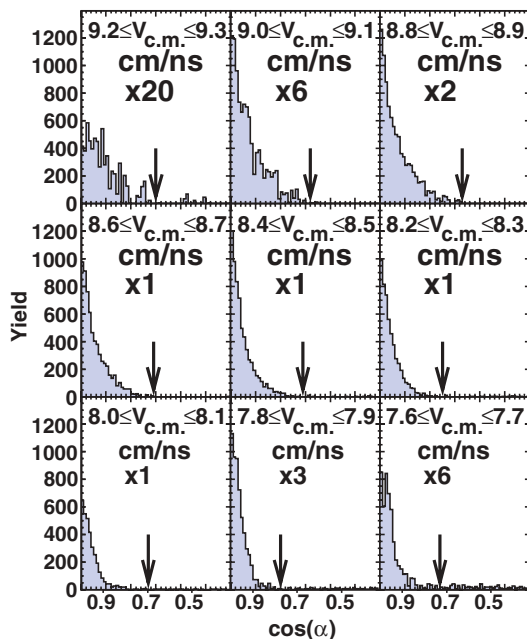


FIG. 10. (Color online) Distributions of $\cos(\alpha)$ corresponding to the difference between the measured backward emission and the simulation of statistical emission for different values of $V_{c.m.}$.

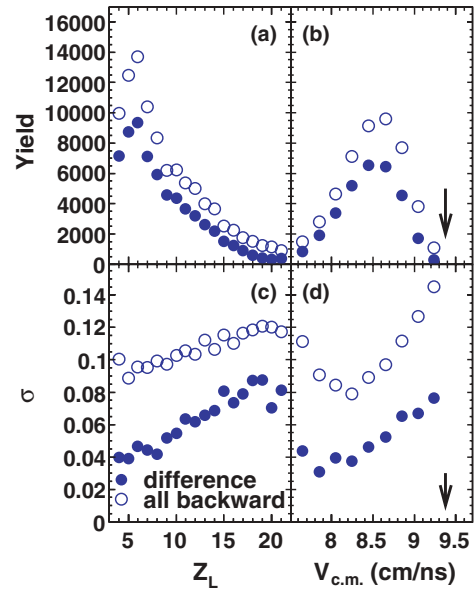


FIG. 11. (Color online) Dependence of the extracted yield and width of the short-lived (dynamical) process on Z_L and $V_{c.m.}$.

are calculated in the range $\cos(\alpha_{\min}) \leq \cos(\alpha) \leq 1$ as indicated in each panel of Figs. 9 and 10 by an arrow. Beyond the integration region shown, the difference spectrum fluctuates around zero due to the statistical uncertainties in the experimental spectrum.

The extracted yields and widths for the short-lived (dynamical) component as a function of Z_L and $V_{c.m.}$ are presented in Fig. 11 as solid circles. With increasing Z_L the yield of the dynamical component first increases slightly from $Z_L = 4$ to $Z_L = 6$, where it reaches a maximum and then decreases systematically. This peak in yield in the vicinity of $Z = 6$ has been previously observed [8,13]; however, the trend of the yield with increasing Z_L is a telling feature. While previous work examined the decay of the dynamical component in terms of the asymmetry of the binary split [12], in the present work we focus on the absolute atomic number of the fragments. The widths of the angular distributions for the dynamical component manifest a steady general increase with Z_L from $\sigma = 0.045$ to 0.095 . As a function of $V_{c.m.}$ one observes that as the PLF* is damped from the beam velocity, the yield of the dynamical channel increases, reaching a maximum at ≈ 8.5 cm/ns. For more damped events, the yield associated with this channel decreases. The degree of alignment, as evidenced by the widths of the angular distributions, increases with damping. For reference, and to demonstrate that the trends for the extracted dynamical component are not an artifact of subtracting the yield associated with the isotropic component, we also present in Fig. 11 the trends observed for the measured backward component as open symbols. It is clearly evident that the overall trends manifested for the dynamical component are already evident for the measured backward yield.

At the simplest level the yield distributions shown in Fig. 11 are influenced by an energy cost associated with producing a fragment. In order to disentangle this dependence, we present a yield ratio in Fig. 12. This ratio is constructed as the additional yield in the backward direction relative

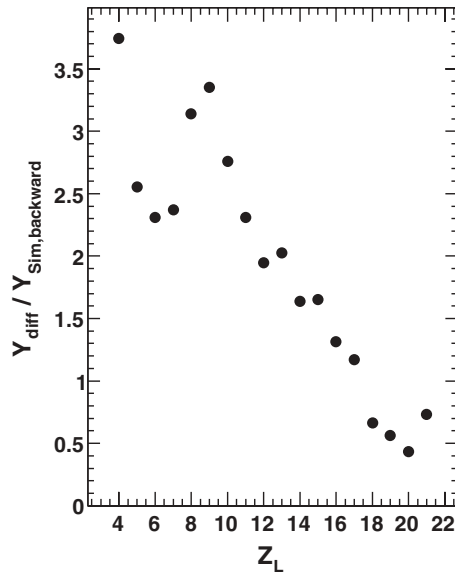


FIG. 12. Ratio of the additional backward yield (Y_{diff}) relative to the isotropic component in the same angular range ($Y_{\text{Sim,backward}}$) as a function of Z_L . See text for details.

to the yield of the isotropic component. This additional yield, Y_{diff} , is determined from the difference between the experimentally measured yield in the backward direction and the isotropic component filtered by the detector acceptance, $Y_{\text{Sim,backward}}$. We associate this isotropic yield with the long-lived statistical emission of the PLF*, while the additional yield we associate with short-lived, nonisotropic emissions. To obtain this estimate of the isotropic backward yield, we have utilized the simulation shown in Figs. 9 and 10. We have utilized the simulated yield over the limits in $\cos(\alpha)$ shown in Fig. 9 to provide the appropriate comparison for the contribution of the isotropic component to the backward direction. In Fig. 12 a peak at $Z_L = 9$ is observed. For $Z_L > 9$ the yield follows a generally decreasing trend. The difference between the yield distribution shown in Fig. 11 and Fig. 12 is striking. The peak at $Z_L = 6$ present in Fig. 11 is not present in Fig. 12, suggesting that this peak arises from energetic factors.

Thus far we have examined the dependence of the dynamical yield on either Z_L or $V_{\text{c.m.}}$. The correlation between the dynamical yield and $V_{\text{c.m.}}$ for different Z_L is shown in Fig. 13. Depicted in Figs. 13(a)–13(e) are the $V_{\text{c.m.}}$ distributions for both forward (open symbols) and backward (closed symbols) emission. As $V_{\text{c.m.}}$ decreases from beam velocity the yield for both forward and backward emission initially increases at a similar rate. For larger dissipation the yield of forward emission reaches a maximum while the yield of backward emission continues to rise. For $Z_L \leq 10$ the yield for backward emission exceeds the yield of forward emission by more than a factor of 2. These $V_{\text{c.m.}}$ distributions can be interpreted as the opening of the statistical and dynamical channels of fragment emission with increasing dissipation. The corresponding results of the simulation for forward and backward emission are shown as the dashed and solid lines, respectively. As expected, the simulation provides a good

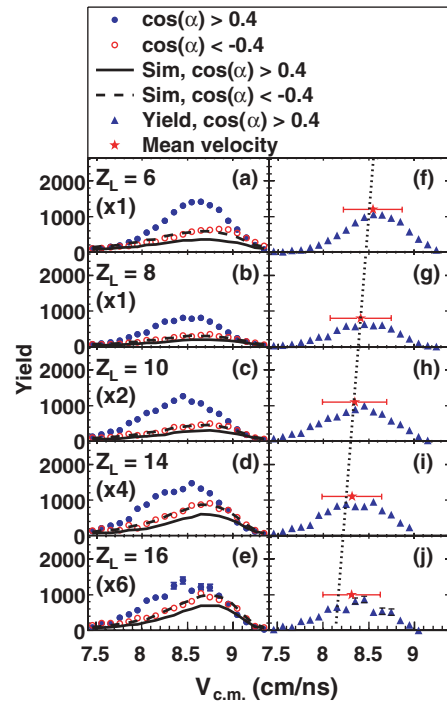


FIG. 13. (Color online) (Left column) Distributions of the center-of-mass velocity associated with both forward (open symbols) and backward (closed symbols) emission together with the results of the simulations for different Z_L . (Right column) Difference distributions constructed from the experimentally measured backward emission together with the filtered simulations in the backward direction for different Z_L . The overall trend of the mean of the difference distributions for $Z_L \leq 14$ is shown as a dotted line. Multiplicative factors used to scale the yield distributions for different Z_L are shown in each panel.

description of the forward emission component. The difference spectra constructed from the experimentally measured backward emission and the simulated backward emission are presented in Figs. 13(f)–13(j). These difference spectra are described reasonably well by Gaussians. The mean value of $V_{\text{c.m.}}$ associated with these spectra is indicated by the solid stars (red) in the right-hand column with the standard deviation of the distribution indicated by the horizontal error bar. For $Z_L \leq 14$ it is clearly evident that $\langle V_{\text{c.m.}} \rangle$ decreases systematically as Z_L increases. This overall trend for $\langle V_{\text{c.m.}} \rangle$ is depicted by the dotted line. The widths in contrast do not exhibit a systematic trend. The trend for $\langle V_{\text{c.m.}} \rangle$ can be understood if the larger Z_L are associated on average with smaller impact parameters, i.e., more damping than smaller Z_L . Close examination of the experimentally measured backward yield reveals that this trend is observed in the experimentally measured distributions and is not an artifact of the difference spectra. It should be noted, however, that the widths of the difference distributions are large compared to the shift of the centroid undoubtedly indicating that the dynamical decay for a given Z_L proceeds from a broad distribution of impact parameters. For the largest Z_L measured, the dependence of $\langle V_{\text{c.m.}} \rangle$ on Z_L appears to saturate.

IV. LANGEVIN SIMULATIONS

In order to better understand the experimental features observed in this reaction we have constructed a simple model to describe the binary splitting of the PLF*. In this one-dimensional model the separation of the Z_L fragment from the initial PLF* is represented by stochastic evolution on a potential energy surface. This surface accounts for the Coulomb and nuclear interaction of the Z_L and Z_H fragments as well as the Coulomb interaction with the TLF*. The potential energy is parameterized by

$$V(x) = -(x - c)(x + c) \left(\frac{x}{d}\right)^2 + \sum_{i=1}^2 e^2 \frac{(Z_{\text{TLF}^*})(Z_i)}{R_i}, \quad (1)$$

where x is the reaction coordinate. The constants c and d , which define the potential and determine the location of the barriers, were chosen to provide reasonable barriers in the case of α evaporation. The second term in the potential describes the interaction of Z_H and Z_L with the TLF* at a distance R_{TLF^*} between the center of mass of the PLF* system and the TLF*. The asymmetry of the barrier heights in the forward and backward direction is caused by the interaction with the TLF*. Values of the reaction coordinate, x , beyond the saddle point can be viewed as the separation distance between Z_L and the center of mass of the parent system. As preformation of the emergent fragment is not considered, the meaning of the coordinate inside the saddle point should be taken as a generalized reaction coordinate. Nonequilibrium population of this coordinate may originate from the collision dynamics. Such nonequilibrium conditions are often observed in transport models as the trailing nuclear material belonging to the PLF*.

The evolution of the system from its initial configuration is described within a Langevin approach. The experimentally observed preference for backward emission over forward emission suggests the persistence of the initial configuration indicating that the motion is overdamped rather than underdamped. Consequently, we work within the high friction limit and within this schematic model we ignore inertial terms. From its initial position on the potential the change in the position of the particle is given by

$$\Delta x = \frac{F \Delta t}{\beta} + k \sqrt{\frac{2T \Delta t}{\beta}}, \quad (2)$$

where Δt is a time step of 0.05 zs (1 zs = 1.0×10^{-21} s). The leading term describes the influence of the potential on the particle's motion with the force due to the potential represented by F . Friction experienced by the particle is given by β . The second term describes the impact of thermal motion on the particle's trajectory. The fluctuating term k is taken to be a Gaussian of unit width centered on zero with the magnitude of the thermal motion scaled for each time step by the temperature T and the friction β .

Displayed in Fig. 14 are potentials associated with various asymmetric splits of the PLF*. Each potential shown is calculated at a distance R_{TLF^*} of 28 fm. The higher barrier observed for $x < 0$ is due to the interaction of Z_H and Z_L with the TLF*, hence the barrier for $x < 0$ corresponds to the barrier governing backward emission. The saddle point

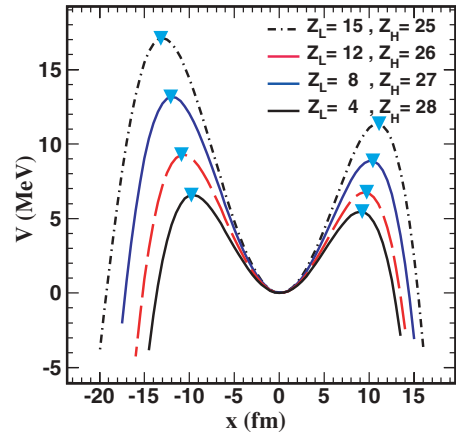


FIG. 14. (Color online) Potentials describing the interaction of the Z_L - Z_H system in the Coulomb field of the TLF*. Potentials shown are relative to the potential energy for $x = 0$.

for each barrier is indicated by a triangle. Early statistical emission from an equilibrated source would favor forward rather than backward emission due to the larger barrier heights in the backward direction. Within the context of the model, the initial population along the reaction coordinate must favor large negative values of x to explain the preferential backward emission.

For each Z_L considered we have taken the average value of Z_H from the experimental data. Consistent with previous work [22,38], we have taken the spin of the rotating source to be $40 \hbar$ and the temperature to be 4 MeV. We have performed calculations at two different values of β , namely 0.2 and 0.4. Then, for a given Z_L and Z_H pair we have calculated the interaction potential at an initial R_{TLF^*} distance of 28 fm. At this distance one can neglect the nuclear influence of the TLF*. Starting from this larger separation of PLF* and TLF* rather than a touching configuration of TLF*- Z_L - Z_H means that the extracted emission times are slightly shorter than the scission-to-scission times by an estimated 0.1–0.2 zs. The time evolution of the particle on the potential, namely Z_L , is then followed starting from an initial displacement x . In order to reproduce the preferential yield backward the particle is displaced by a distance $x < 0$ on the potential. As the particle evolves on the surface, the potential is recalculated at each time step due to the increasing distance between the PLF* and the TLF* and the rotation of the PLF*. In each time step the PLF* separates from the TLF* with a velocity of 7.5 cm/ns. The time and angle at which the particle escapes the barrier is recorded.

The angular distributions predicted by this schematic model for different initial positions are presented in Fig. 15 for $Z_L = 4$ and $Z_L = 13$. One observes a clear sensitivity to the initial position of the fragment on the potential. Larger initial displacements from the equilibrium position result in more peaked angular distributions. This result is not surprising since larger initial displacements result in shorter average times for the particle to surmount the barrier. In the case of $Z_L = 4$, the best agreement with the experimental angular distribution occurs for an initial displacement of -13.25 fm. Although this initial displacement lies outside the saddle point, the random

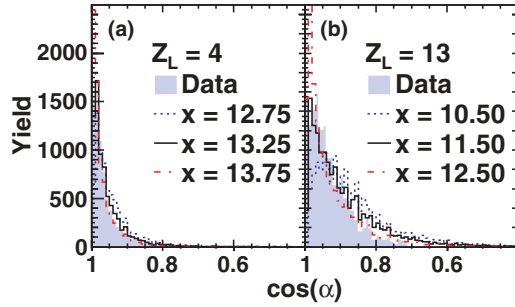


FIG. 15. (Color online) Comparison of difference angular distributions of $Z_L = 4$ and 13 with the results of the Langevin model. Calculations were made with $\beta = 0.4$.

motion of the particle results in a noninstantaneous lifetime. For the heavier fragment $Z_L = 13$, the initial displacement required to reproduce the measured angular distribution is somewhat less, $x = -11.5$ fm.

Since the position of the barrier changes with the specific fragment pair Z_L/Z_H considered it is more useful to consider the initial displacement relative to the backward barrier. The dependence of this quantity $x-x_B$ on Z_L is examined in Fig. 16. The error bars shown correspond to the best estimate of the uncertainty involved in describing the measured angular distributions. For a given choice of β , the initial displacement from the barrier increases essentially linearly with Z_L . A larger value of the friction results in shifting $x-x_B$ to smaller values for a given Z_L . It is interesting to note that for the lightest Z_L , the measured angular distributions are only described by $x-x_B < 0$ namely displacements outside the barrier. For $\beta = 0.4$, we deduce that $Z_L \leq 8$ fragments have initial positions outside the barrier while $Z_L \geq 9$ fragments have positions inside the barrier. It should be recalled that for this fragment atomic number, $Z_L = 9$, the relative yield of the dynamical component reached a maximum (Fig. 12).

From the schematic model presented we also extract the average emission time. The dependence of this lifetime on the charge asymmetry η or Z_L is shown in Fig. 17 under

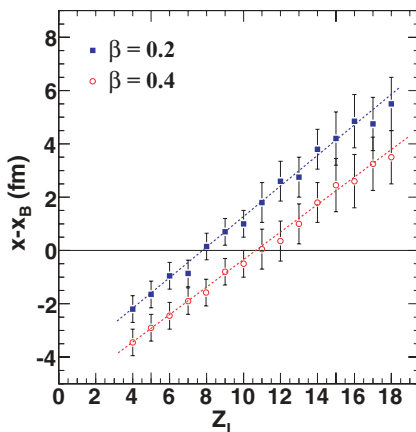


FIG. 16. (Color online) Initial displacement from the top of the backward barrier necessary to reproduce the measured angular distributions for different Z_L fragments. Results are shown for both $\beta = 0.2$ and 0.4.

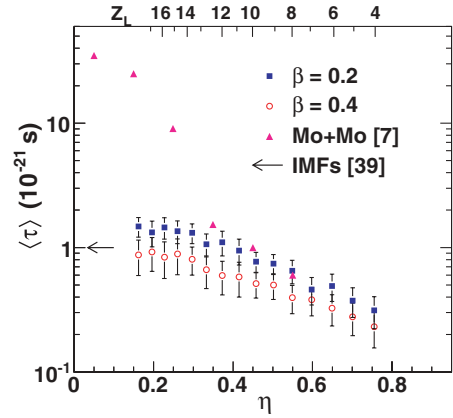


FIG. 17. (Color online) Mean lifetime extracted as a function of the asymmetry of the split (or equivalently Z_L). The arrow indicates the emission time scale extracted for midvelocity IMFs in the reaction $^{116}\text{Sn} + ^{93}\text{Nb}$ at $E/A = 29.5$ MeV [39]. The triangles represent the scission-to-scission lifetime extracted as a function of charge asymmetry in the reaction $^{100}\text{Mo} + ^{100}\text{Mo}$ at $E/A = 18.7$ MeV [7].

different assumptions of β . Presenting the data as a function of η allows comparison with previously published data. The charge asymmetry η is defined as $\eta = \frac{(Z_H - Z_L)}{(Z_H + Z_L)}$. For $\beta = 0.4$, with increasing charge asymmetry the average emission time decreases from a maximum of 0.9 to 0.25 zs. Reducing the spin of the PLF* from $40 \hbar$ to $30 \hbar$ resulted in a 25% increase in the extracted emission times. A smaller value of the friction $\beta = 0.2$ results in slightly larger values of the emission time, 0.3 to 1.5 zs. For reference we also show the comparable scission-to-scission times extracted in previous work [7]. In Ref. [7], in-plane angular distributions were fit with a functional form in which one free parameter was the average rotation of the dinuclear system prior to decay; an estimate of the rotational frequency is then used to calculate the average lifetime. In the range $\eta = 0.3-0.6$ mean emission times extracted for the Mo + Mo system are in reasonably good agreement with the present work. In the case of the Mo + Mo system for $\eta < 0.25$ a dramatic increase in the emission time is observed. This dramatic increase in emission time is *not* observed in the present data set where the emission times for $\eta < 0.3$ increase smoothly from the trend observed for more asymmetric decays. These shorter times extracted for more symmetric splits may indicate that the distribution of transient deformations produced in the present data differs from that in Mo + Mo.

V. CONCLUSIONS

We have examined the characteristics of dissipative binary collisions in which a large projectile-like fragment (PLF) with $21 \leq Z \leq 55$ is measured in the angular range $3^\circ \leq \theta_{\text{lab}} \leq 7^\circ$ following the reaction $^{124}\text{Xe} + ^{124}\text{Sn}$ at $E/A = 50$ MeV. This work focuses on the nature of a subset of these events in which in addition to the heavy fragment a lighter fragment with $Z \geq 4$ is detected in the same angular range. These binary events can be categorized based on the direction of emission of the lighter fragment: either forward emission (away from the

TLF) or backward emission (toward the TLF). The center of mass of the fragment pair manifests significantly more velocity damping than the PLF for inclusive events. The degree of velocity damping for backward emission is similar to that of forward emission though slightly larger.

From the measured angular distribution it is clear that backward decays are both more probable and more strongly aligned than forward decays. With increasing Z_L , the features of increased yield in the backward direction and strong alignment diminish. However, even nearly symmetric splits of the PLF* manifest these two features. For the least dissipative collisions the angular distributions measured are nearly forward/backward symmetric. For slightly larger damping one observes the onset of increased yield in the backward direction and aligned decay. These features become more pronounced with increased damping. The enhanced yield observed in the backward direction can be interpreted as due to the superposition of both standard long-lived statistical decay, which is responsible for the forward emission, and an additional short-lived dynamical component.

Using the forward emission as a reference, we extract the angular distribution of the short-lived (dynamical) component and report the evolution of the yield and width with Z_L and $V_{c.m.}$. The yield distribution of the short-lived (dynamical) component relative to the long-lived statistical component in the same angular range follows different trends for $Z_L < 9$ and $Z_L \geq 9$ suggesting a possible transition in production for fragments of that atomic number. For a fragment of a given Z_L , at low damping forward and backward emission are equally probable. With increasing damping, however, backward emission becomes dominant over forward emission. For $Z_L = 10$ this short-lived dynamical yield surpasses the long-lived statistical yield by a factor of three. We interpret the behavior of the yield as a function of $V_{c.m.}$ as the opening of the statistical and dynamical channels with increased damping/excitation.

To assess the degree of equilibration for such binary decays we have examined the isotopic distributions and constructed the average neutron excess as described by $\langle N \rangle - Z$. This neutron excess has a value of 0.8–1.2 for $Z_L < 9$ and 1.45–1.65 for $Z_L \geq 9$. This sudden jump in $\langle N \rangle - Z$ is another signal for some transition occurring for fragments of this size. We also observe a dependence of the neutron excess on the emission angle of Z_L , possibly indicating sensitivity to nucleon transport between Z_L and Z_H on a time scale significantly shorter than the rotational period. Alternatively, one may construe these observations as indicating that different regions of the angular distribution are populated by sources of different composition.

By using a schematic one-dimensional Langevin model we extracted the initial deformation of the PLF* relative to the emission barrier for different Z_L . Independent of the friction β assumed, an essentially linear trend of initial deformation with Z_L is deduced. The smallest fragments are produced at or beyond the barrier with the largest fragment size produced at the barrier depending on the magnitude of the friction. Within this simple model the extracted emission time scale for different asymmetric splits of the short-lived dynamical component ranges from 0.25– 1.5×10^{-21} s. While for more asymmetric splits ($\eta > 0.3$) these extracted lifetimes agree

well with previously published data [7], for smaller η we measure significantly shorter emission times than those previously reported. The smooth systematic trend measured for the present work for all η suggests that for the present reaction even near-symmetric splits have a significant nonequilibrium (dynamical) character. These extracted scission-to-scission times are comparable in magnitude to the time scale for midvelocity emission of intermediate mass fragments ($3 \leq Z \leq 20$) of 300 fm/c as indicated by the arrow in Fig. 17 [39]. However, this previous work did not explore the dependence of the emission time scale on the atomic number of the emitted fragments. Consequently, this extracted time scale most likely reflects the emission time of the lightest fragments as they are the most abundant. In the present work, we observe a smooth evolution of the emission time scale from 1.5 zs (~ 450 fm/c) for the smallest measured asymmetries to ~ 0.3 zs (~ 90 fm/c) for the most asymmetric splits.

To summarize, we have learned about the properties of aligned breakup of an excited PLF* produced in noncentral collisions. From the backward peaked angular distributions of these decays we have deduced a short lifetime for the rotating, deformed PLF*. It is noteworthy that this short-lived dynamical yield is not restricted to fragments with $Z_L \leq 10$, previously thought of as “neck fragments,” but persists for fragments as large as $Z_L = 18$, i.e., near symmetric splits of the PLF*. The short lifetime ($< 1.5 \times 10^{-21}$ s) of these more symmetric splits follows a smooth systematic trend from more asymmetric splits indicating that even production of these large fragments is impacted by the collision dynamics. The dependence of the angular distribution on velocity damping indicates that at least a minimum damping is necessary to access this decay mode. This minimum damping is larger than that necessary to open the statistical channel. Presumably, this minimum damping is correlated with a minimum overlap of the projectile and target nuclei. Beyond this minimum damping, the yield of the dynamical mode increases with increasing damping. Within the context of a schematic model we deduce that the size (Z_L) of the dynamically produced fragment is related to the degree of transient deformation relative to the emission barrier. A more complete understanding of this phenomenon will require comparison of the experimental data with more complete theoretical models which include both the nonequilibrium populations produced by the collision dynamics as well as the evolution of these populations on more realistic potentials. In addition, the success of such models will depend on their ability to accurately account for the presence of inertial terms and the coupling of thermal modes to the collective degrees of freedom.

ACKNOWLEDGMENTS

We wish to acknowledge the support of the GANIL staff in providing the high-quality beams that made this experiment possible. We are especially grateful to Y. Georget, B. Jacquot, and V. Morel. This work was supported by the US Department of Energy under Grant No. DEFG02-88ER-40404 (IU). Collaboration members from Université Laval recognize the support of the Natural Sciences and Engineering Research Council of Canada.

- [1] J. P. Theobald *et al.*, Nucl. Phys. **A502**, 343 (1989).
- [2] D. E. Fields *et al.*, Phys. Rev. Lett. **69**, 3713 (1992).
- [3] S. L. Chen *et al.*, Phys. Rev. C **54**, R2114 (1996).
- [4] D. Poenrau and W. Greiner, *Nuclear Decay Modes* (CRC Press, Boca Raton, FL, 1996).
- [5] T. Bredeweg *et al.*, Phys. Rev. C **66**, 014608 (2002).
- [6] E. D. Filippo *et al.*, Phys. Rev. C **71**, 044602 (2005).
- [7] G. Casini *et al.*, Phys. Rev. Lett. **71**, 2567 (1993).
- [8] C. P. Montoya *et al.*, Phys. Rev. Lett. **73**, 3070 (1994).
- [9] J. Töke *et al.*, Phys. Rev. Lett. **75**, 2920 (1995).
- [10] J. Töke *et al.*, Phys. Rev. Lett. **77**, 3514 (1996).
- [11] E. Plagnol *et al.*, Phys. Rev. C **61**, 014606 (1999).
- [12] F. Bocage *et al.*, Nucl. Phys. **A676**, 391 (2000).
- [13] B. Davin *et al.*, Phys. Rev. C **65**, 064614 (2002).
- [14] J. Łukasik *et al.*, Phys. Rev. C **66**, 064606 (2002).
- [15] L. Gingras *et al.*, Phys. Rev. C **65**, 061604(R) (2002).
- [16] J. Colin *et al.*, Phys. Rev. C **67**, 064603 (2003).
- [17] S. Hudan *et al.*, Phys. Rev. C **70**, 031601(R) (2004).
- [18] S. Piantelli *et al.*, Phys. Rev. C **76**, 061601 (2007).
- [19] R. Moustabchir *et al.*, Nucl. Phys. **A739**, 15 (2004).
- [20] A. Mangiarotti *et al.*, Phys. Rev. Lett. **93**, 232701 (2004).
- [21] A. Botvina *et al.*, Phys. Rev. C **63**, 061601(R) (2001).
- [22] R. Yanez *et al.*, Phys. Rev. C **68**, 011602(R) (2003).
- [23] T. Padaszynski *et al.*, Nucl. Instrum. Methods A **547**, 464 (2005).
- [24] MicronSemiconductor, www.micronsemiconductor.co.uk.
- [25] C. Metelko *et al.*, Nucl. Instrum. Methods A **569**, 815 (2006).
- [26] B. Davin *et al.*, Nucl. Instrum. Methods A **473**, 302 (2001).
- [27] I. Tilquin *et al.*, Nucl. Instrum. Methods A **365**, 446 (1995).
- [28] J. Huizenga and W. Schroder, *Treatise on Heavy Ion Science* (D. A. Bromley, 1984), Vol. 2.
- [29] D. Doré *et al.*, Phys. Lett. **B491**, 15 (2000).
- [30] D. Doré *et al.*, Phys. Rev. C **63**, 034612 (2001).
- [31] V. Viola *et al.*, Phys. Rev. C **31**, 1550 (1985).
- [32] R. Charity *et al.*, Phys. Rev. Lett. **56**, 1354 (1986).
- [33] G. Souliotis *et al.*, Phys. Rev. C **68**, 024605 (2003).
- [34] V. Henzl, Ph.D. thesis, Czech Technical University, Prague (2005).
- [35] S. Piantelli *et al.*, Phys. Rev. C **74**, 034609 (2006).
- [36] R. J. Charity, Phys. Rev. C **58**, 1073 (1998).
- [37] J. Normand, Ph.D. thesis, Université de Caen, France, 2001.
- [38] J. C. Steckmeyer *et al.*, Nucl. Phys. **A686**, 537 (2001).
- [39] S. Piantelli *et al.*, Phys. Rev. Lett. **88**, 052701 (2002).